Journal of Advanced Joining Processes 8 (2023) 100167

Contents lists available at ScienceDirect

Journal of Advanced Joining Processes

journal homepage: www.sciencedirect.com/journal/journal-of-advanced-joining-processes

Finite element modelling of transient behaviours and microstructural evolution during dissimilar rotary friction welding of 316 austenitic stainless steel to A516 ferritic steel

Amborish Banerjee *, Laurie da Silva, Salaheddin Rahimi

Advanced Forming Research Centre (AFRC), University of Strathclyde, 85 Inchinnan Drive, Inchinnan, Renfrewshire, PA4 9LJ, UK

ARTICLE INFO

Keywords:
Inertia friction welding
Finite element simulation
Temperature distribution
Dissimilar welding

ABSTRACT

Inertia friction welding (IFW) is a near-net-shape joining process that produces high-integrity welds. The transient nature of this joining process necessitates the availability of reliable computational models to predict the evolution of temperature and deformation throughout welding. In this study, a thermo-mechanical finite element (FE) model, based on an adaptive remeshing technique, is proposed to simulate dissimilar joining of A516 ferritic steel and 316L austenitic stainless steel (SS). The results of FE model were evaluated and verified via comparing the shape/size of the flash, upsetting load and angular velocity profile of a physical weld produced by IFW trials. A good agreement was achieved between the appearance of the weld/flash and those predicted by the FE model, thus verifying the predicted temperature and strain distributions. The microstructural features across different weld regimes were also examined to correlate the concomitant changes with the simulated temperature profile.

Introduction

Dissimilar welds of SS to ferritic steel are highly desirable for applications in nuclear power plants, since they facilitate design flexibility at reduced cost, and provide fit-for-purpose components (i.e., with tailored mechanical strength and high temperature resistance) (Wang et al., 2013). Austenitic SS are used for critical applications at high-temperatures, such as reheaters and superheaters, while ferritic steels are used in relatively lower-temperatures under higher demands for mechanical strength. Welding of SS to ferritic steel is usually performed via conventional methods, e.g., electron-beam and fusion welding (Ghosh et al., 2018; Rathod et al., 2015). However, due to difference in thermal expansion of the two materials, dissimilar welds are vulnerable to solidification cracks and typically contain metallurgical defects. Typically, during conventional welding of ferritic steels to stainless steels, buttering layers (~ 6–8 mm) of sacrificial nickel-based alloys are used to compensate for the mismatch introduced by the differential gradient in thermal expansion and other physical, mechanical and metallurgical properties between the two materials (Sunilkumar et al., 2020). Setting up this tri-metallic configuration is time consuming, and most importantly prone to hot cracking. Owing to the nature of the process, these challenges are eliminated by solid-state welding where the components are joined below their melting temperatures. IFW is a variant of rotary friction welding, where tubular components are joined under the application of friction and forge forces. An extensive description of this process including different stages of conditioning, forging and cooling is reported elsewhere (Banerjee et al., 2021, 2022).

While efforts are ongoing to comprehend material behaviors during IFW (Tung et al., 2019), evolution of transient thermo-mechanical properties, especially for dissimilar materials needs further attention due to relative differences in the inherent thermal and mechanical properties. Thus, developing computational models for predicting temperature and stress-strain fields becomes vital. It is well understood that in IFW process, the weld interface experiences an abrupt increase in the temperature for a small fraction of time because of the enormous frictional heat (Yang et al., 2015). Therefore, determining the appropriate friction behavior (i.e. friction coefficient) is one of the key ingredients to effectively simulate the IFW process. Although previous reports are available on the FE simulation of dissimilar steels (Bennett et al., 2013; El-Hadek, 2014), defining the friction parameters during IFW demands further understanding. For instance, some studies have considered the friction coefficient to be dependent on pressure, speed and temperature (Balasubramanian et al., 1999; Moal and Massoni, 1995), however,

* Corresponding author.
E-mail address: amborish.banerjee@strath.ac.uk (A. Banerjee).

https://doi.org/10.1016/j.jajp.2023.100167

Available online 15 November 2023

determining the temperature at the interface during the on-going welding process is unfeasible. A more likely approach is the slip-stick friction model (Geng et al., 2019) which states that the sliding friction (based on the Coulomb's friction law) is dominant when the friction stress is lower than the shear stress, otherwise shear friction is presiding. This approach has been widely used by many researchers (Maalekian et al., 2008; Cerjak et al., 2005; Lee et al., 2001), where the sliding and sticking friction coefficients were determined based on the recrystallization temperatures. However, considering the differences in compositions and recrystallization temperature, this methodology may not be appropriate for simulation of welding between dissimilar materials. Similarly, assuming a constant friction coefficient (i.e., either shear or coulomb friction) during IFW also leads to unrealistic results. This is governed by the nature of the process where friction coefficient is significantly high at lower temperatures and vice versa (i.e., low at higher temperatures) due to the temperature dependent mechanical properties of the materials such as resistance to deformation.

In this study, a coupled thermo-mechanical and torsional FE model was developed to determine temperature and deformation distributions in type 316L austenitic SS and A516 ferritic steel during the conditioning and forging stages of the IFW. The cooling stage has not been modeled in this study. The model includes a comprehensive implementation of defining friction coefficient based on a constitutive equation, an adaptive remeshing technique, and heat transfer coefficients. The developed model is helpful to understand the critical process parameters affecting the structural integrity of the welds, aiding optimization of industrial scale welding.

FE modelling and microstructural characterisation

An axisymmetric 2.5D thermo-mechanical torsional FE model was developed using DEFORM software to predict in-process temperature distribution and deformation behavior during the IFW. Fig. 1a shows the FE setup including the mesh size, thermal and loading boundary conditions. The workpieces were modeled as pure-plastic bodies, one attached to the welding machine's flywheel and the other to a fixture, considering a sticking condition. The axial force and velocity were set as those used in the physical trial described later. An adaptive remeshing technique, producing smaller mesh size (0.005 mm) at the weld interfaces was applied to accommodate real-time local deformation. The model was developed to simulate only the heating stage of the process, while the cooling stage which is mainly responsible for the residual stress generation was excluded. The flow curves at different strain rates (0.01 to 10 /s) and temperatures (25–1400 °C) were assigned as input parameters for the FE simulation. The flow stress values of both materials were taken from the JMatPro software and other available database. The yield strengths of both SS316L and A516 steel are provided in Fig. 1b and c, respectively. The changes in the yield point of the A516 as a function of temperature is likely to be due to the phase transformation (i.e., transformation to austenite) at temperatures below 900 °C. For 316 SS, the changes occur at around 600 °C which is the ideal temperature range for the precipitation of different carbides, and this is likely to be the reason for the changes in the yield point. Moreover, the physical properties of both materials were evaluated using the JMatPro software (see Table 1), taking into consideration the nominal chemical compositions. The Poisson's ratio and density of the steel were considered ~0.3 and 7850 kg/m^3, respectively.

In this study, the viscoplastic model defining the material flow and temperature evolutions during conditioning and metal forming stages was implemented. This approach is based on the minimum work rate principle (Zhang et al., 2006) which provides approximate solutions to a differential equation. This model couples the mechanical and thermal effects during the on-going deformation process and is described as

$$\Pi = \int_V E\left(\dot{\varepsilon}_{ij}\right) dV - \int_A \overline{F}_i V_j dS \tag{1}$$

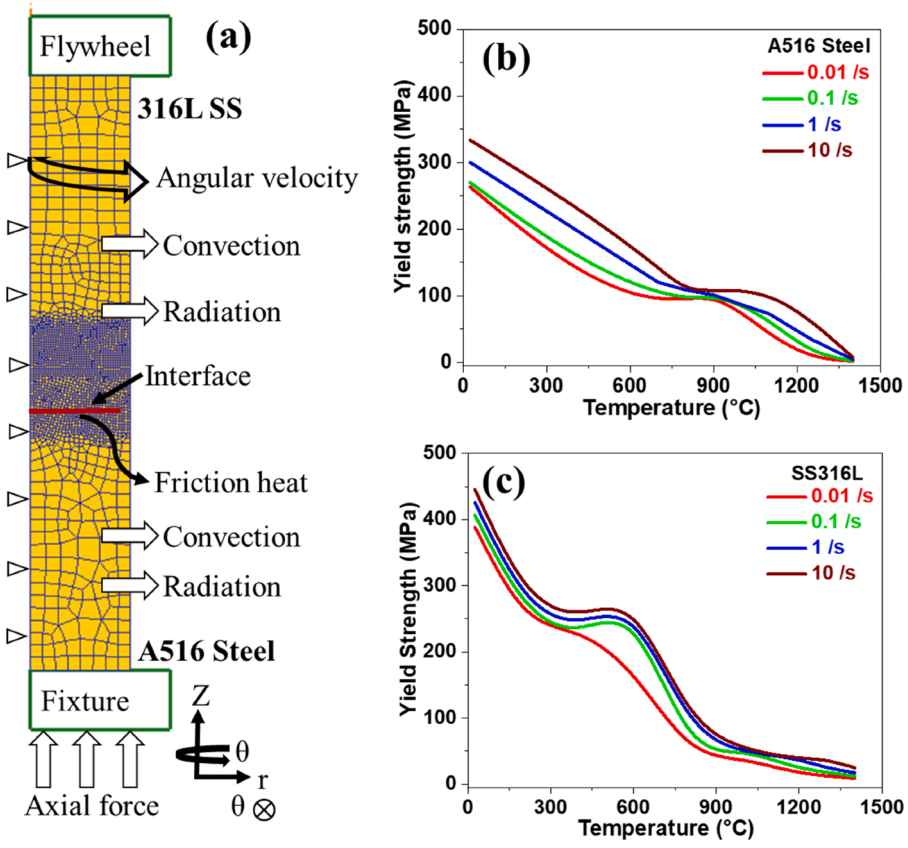

Fig. 1. (a) 2.5D axisymmetric model describing the mesh and boundary conditions, (b) and (c) variation of yield strength of A516 steel and SS316L, respectively.

Table 1
Thermal-mechanical properties of A516 and 316L steels.

Temperature (°C)	Elastic modulus (MPa)		Thermal conductivity (N/sec/°C)		Heat capacity (J/kg°C)	
	316SS	A516	316SS L	A516	316SS	A516
20	192097.8	200454.0	14.35	20.50	3.57	3.59
200	180122.5	194846.5	17.38	22.84	4.07	3.97
400	165874.6	168848.9	20.28	24.90	4.29	4.34
600	151027.5	148378.1	22.70	26.31	4.42	4.85
800	135581	125848.8	24.64	26.89	4.71	7.04
1000	119535.4	105642.3	26.10	28.79	5.41	4.70
1200	102890.4	85245.6	27.08	31.17	6.78	4.86
1400	78621.6	64286.6	27.58	33.55	9.05	5.05

where $E(\varepsilon_{ij})$, V, A, F_i, V_j represent viscoplastic potential, specimen volume, contact area, friction stress and velocity, respectively. For the evaluation of volume incompressibility condition, the variation function is converted to a non-linear algebraic equation by introducing a penalty constant, K (a large positive number), using the FE discretization procedure (Geng et al., 2019), defined as:

$$\delta\Pi = \int_V \overline{\sigma}\delta\dot{\overline{\varepsilon}}dV - \int_A \overline{F_i}\delta v_i dS + \int_V k\dot{\varepsilon}_V\delta\dot{\varepsilon}_V dV \quad (2)$$

where $\dot{\varepsilon}_V = \varepsilon_{ij}$ and δv_i represent strain-rate and an arbitrary variation in Eq. (2), respectively. Eq. (2) is the Lagrangian formulation used in the FE simulation and its solution was obtained using the Newton-Raphson method. The first, second and third terms denote the plastic work, surface tension work and volume change, respectively, while $\dot{\varepsilon}_V = \dot{\varepsilon}_{ij}$ is the volumetric strain-rate and δv_i is the arbitrary variation.

In IFW, a significant increase in the weldability is achieved because of high friction and substantial plastic deformation. The temperature distribution was thereby predicted by performing the heat transfer analysis considering (a) heat transfer between the workpieces and environment, and (b) heat generation at the interface due to friction and plastic deformation. Assuming a homogeneous and isotropic continuum, the non-linear heat conduction equation which is based on energy conversation principle is expressed as follows (Maalekian et al., 2008):

$$\rho C_p \frac{\partial T}{\partial t} = \frac{\partial}{\partial Z_i}\left(k\frac{\partial T}{\partial Z_i}\right) + \rho C_p u\frac{\partial T}{\partial Z_i} + \dot{S}(\alpha\overline{\sigma}\dot{\overline{\varepsilon}}) \quad (3)$$

where ρ, C_p, k, α and T denote density, specific heat, thermal conductivity, thermal expansion coefficient and instantaneous temperature of the material. The term Z_i indicates the distance from the weld interface. The term $\rho C_p u\frac{\partial T}{\partial x_i}$ denotes the shortening of workpiece during IFW, and $(\dot{S})$ represents heat generation rate where $\overline{\sigma}$ and $\dot{\overline{\varepsilon}}$ are the effective stress and strain-rate, respectively.

The heat transfer between the workpieces and environment was defined considering both convection (i.e., defined by Newton's cooling law) and radiation (i.e., defined by the Stefan–Boltzmann equation):

$$q = h(T_b - T_o) + \in \left(T_b^4 - T_o^4\right) \quad (4)$$

where q, h and $\in$ denote heat flux, heat-transfer coefficient (25 W/m^2/k) and emissivity (0.7), respectively. T_b and T_o represent the surface and ambient temperatures. The first part of the equation represents the convection phenomenon and the latter the radiation loss. The recorded ambient temperature during the actual weld trial was ~20 °C.

The friction at the weld interface was introduced by using a velocity and energy based representative simulation where the friction coefficient was determined by performing an inverse analysis of heat generation based on the experimental flywheel rundown data (i.e., deceleration curve) (Cerjak et al., 2005). The friction coefficient (μ_n) was then defined using a constitutive equation as a function of time (Δt) considering a constant pressure as Eq. (5) (Lee et al., 2001; Vill, 1962):

$$\mu_n = \eta\frac{E_{n+1} - E_n}{-\omega_n \Delta t p\left(\frac{2\pi}{3}[r^3]\right)} \quad (5)$$

where, η, E, ω_n, p and r denote the efficiency factor, energy, angular velocity, pressure and radius, respectively. The subscripts n and n+1 denote the current and subsequent time. The bearing friction losses during the IFW were considered by defining an efficiency factor $(\eta) \approx 0.85$. Fig. 2a shows the variation in the friction coefficient as a function of temperature.

For the weld trial, cylindrical bars of SS316L and A516 steel, with 50 mm diameter and 100 mm length, were welded at 1805 RPM and 15 MPa forge pressure. The flywheel energy and inertia during the IFW process were 331947334 Nmm and 18601 Nmms^2, respectively. Following IFW, the longitudinal cross-section of the weld was examined by optical and scanning electron microscopy (OM, SEM) and electron backscattered diffraction (EBSD) for microstructural characterizations. The EBSD scan was performed under 15 kV accelerating voltage with 0.2 μm step size using a FEI Quanta-650 field-emission gun SEM. The OM and SEM micrographs showed the presence of pearlite and ferrite in the as-received microstructure of the A516 steel (Fig. 2b and d). Similarly, the 316L stainless steel exhibited polyhedral austenite grains with annealing twins as shown in Fig. 2c and e.

Results and discussion

The predicted temperature and stress fields during the IFW (Fig. 3) look asymmetrical due to the difference in the thermo-physical/mechanical properties of these materials. The temperature evolution at different weld times (Fig. 3a–f) showed an increase during the initial period (within 3 s) due to frictional shear stress and high heat flux. The highest temperature predicted at the weld interface of A516 steel (~1352 °C) was marginally higher than that of the SS316L (~1339 °C). Based on chemical compositions, the melting (T_m) and recrystallization temperatures ($0.5T_m$) of the A516 ferritic steel were calculated to be ~1457 °C and 728.5 °C, respectively, and those for 316L austenitic SS were calculated to be ~ 1395 and 697 °C, respectively. These imply that the welding occurred above the materials' recrystallization temperatures and below their melting points. The peak temperature was reached ~ 5 s, thereafter the temperature profile showed a decreasing trend, this is due to the decrease in the induced frictional heat. In general, with increasing temperature the material softens and a decrease in the friction coefficient is observed. This resulted in a decrease in the frictional heat which is manifested in the form of temperature decrease. On the other hand, the peak stress (410 MPa) was observed at ~ 10.5 s which can be correlated with the flywheel rundown data (see Fig. 4c). As evident, the flywheel movement was ceased at ~ 10 s, and no further rotation was occurred between the welding parts. This implies that from this point onward (i.e., 10 s), no energy was imparted by the flywheel to the weld and hence no deformation occurred in the weld components, thereby resulting in an overall decrease in the stress field. With further progress of the IFW, the weld-regime became viscoplastic resulting in expelling hot materials in form of flash. The flash was more prominent at the interfacial regions of A516 steel owing to its lower yield strength than SS316L. During the initial few seconds of the IFW, complete contact between the faying surfaces is not attained due to the uneven distribution of angular velocity (i.e., slower at the centre and faster towards the edge). This leads to a varying frictional heat distribution from the centre to the edge, leading to higher temperatures near the edge. Also, a decrease in the effective stress was observed in the vicinity of the weld interface (Fig. 3g–l) due to temperature rise which successively led to a decrease in flow stress. Moreover, higher stresses were generated away from the weld interface due to the presence of adjacent colder materials, resisting plastic deformation.

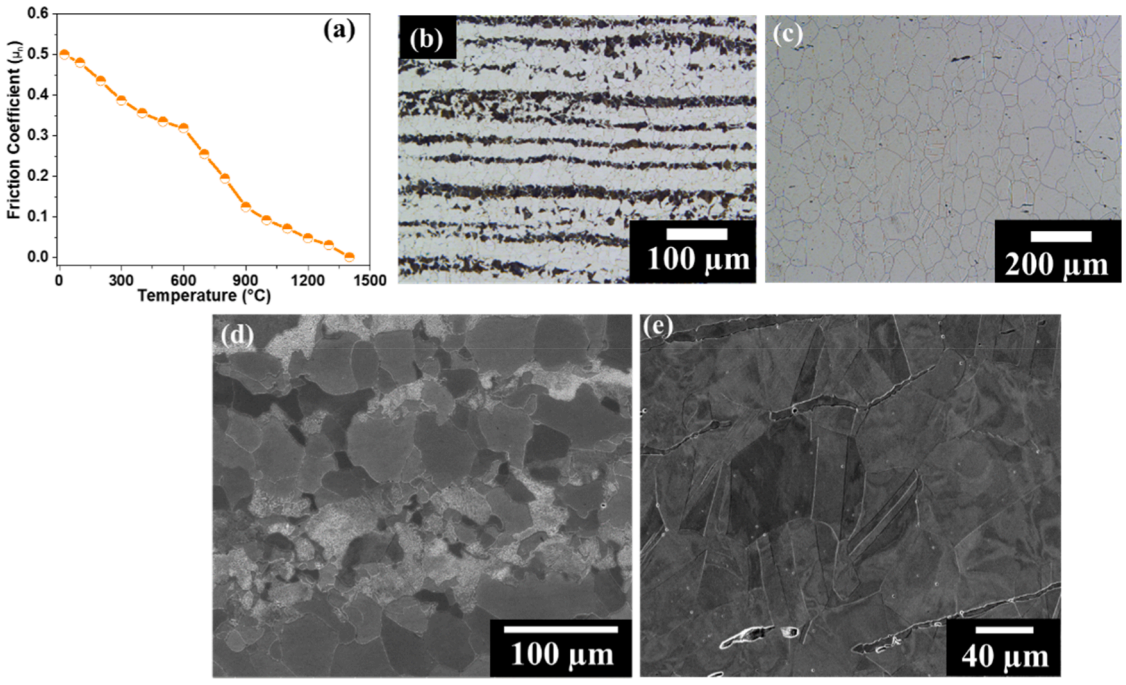

Fig. 2. (a) Variation in the friction coefficient variation, (b) and (c) OM of the as-received A516 and 316L stainless steel respectively, (d) and (e) SEM micrographs of the A516 and 316L stainless steel, respectively.

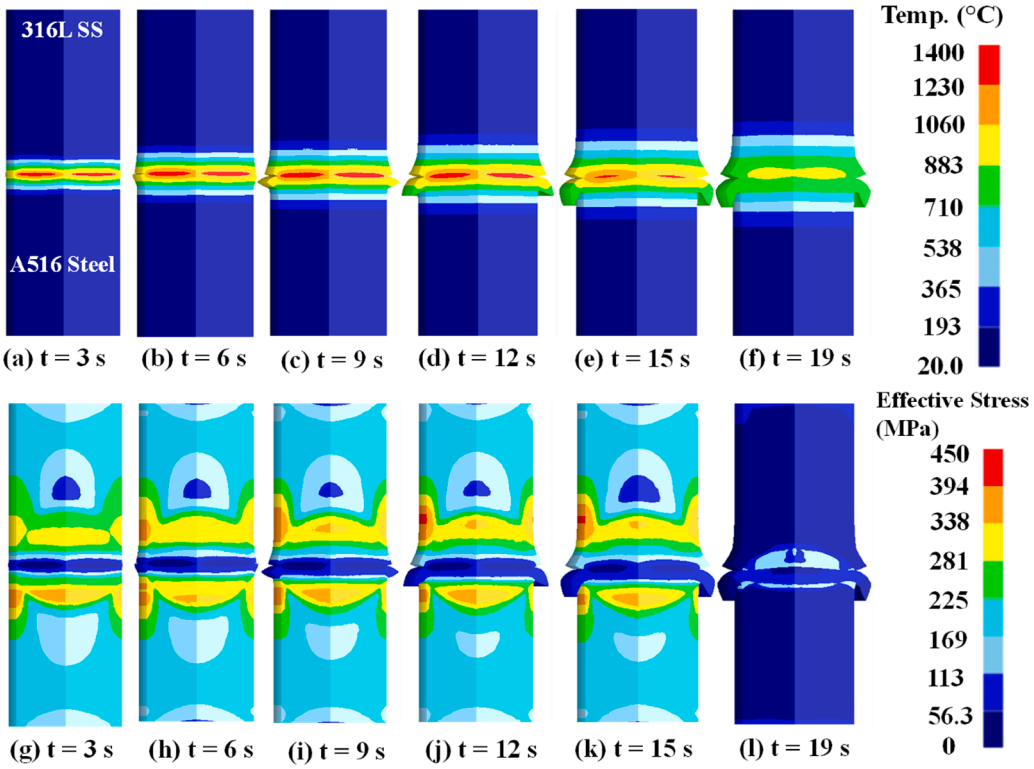

Fig. 3. FE predicted temperature and stress fields during IFW of SS316L and A516 steels at different time steps (a) – (f) temperature, and (g) – (l) effective stress.

The simulated results were verified by an experimental trial. Fig. 4a and b show the flash profiles obtained by the FE model and the physical trial, showing an excellent agreement. The lengths of the predicted and experimental flash were ~13.9 and 14 mm, respectively (0.7 % error) which validates the suitability of the developed FE model to simulate IFW of dissimilar steels. Retardation of the flywheel angular velocity (Fig. 4c) exhibited a rational match between the predicted and measured values. Similarly, the simulated upset (~9.52 mm) was in close agreement (see Fig. 4d) with the experimental value (~8.90 mm). However, a mismatch was observed between the predicted and experimentally obtained upset curves, which might have been caused by heat and energy losses via the fixture and the workpiece.

The distinctive microstructures and EBSD maps of the weldment across different zones are provided in Fig. 5 to correlate the temperature

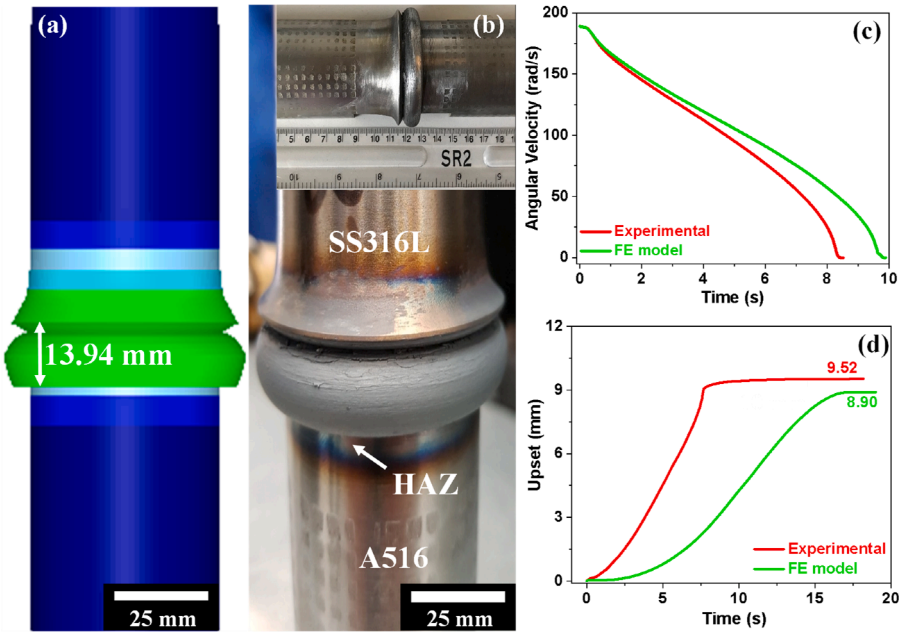

Fig. 4. Comparison between experimental and simulated results (a) and (b) images of predicted and experimental flash, respectively, (c) flywheel run-down profile, and (d) upset after weld completion.

evolution with the microstructural features. Fig. 5a depicts a fully penetrated defect-free weld, with the different regions of the weld highlighted based on microstructural observations. The width of the WZ in SS316L was narrower than that of A516 steel by ~400 μm. The WZ of A516 steel shown in Fig. 4b consisted of martensite and granular bainite compared to ferrite and pearlite in the microstructure of the base material (BM). The calculated upper and lower critical transformation temperatures (Ac_1 and Ac_3) for the A516 ferritic steel were ~ 721.3 °C and 819.4 °C. Therefore, the formation of martensite and bainite in the WZ imply that the temperature was at or above the Ac_3 temperature (~ 819.4 °C). The microstructure of 316L (Fig. 5e) contained small equiaxed austenite grains with average grain size of 9 ± 0.5 μm while the average grain size of austenite in the BM was ~ 40 μm. This indicates that the BM experienced severe shear deformation and underwent dynamic recrystallization, which then transformed to refined austenite grains due to the high heat dissipation (or cooling) rate. Note that due to the high nickel (10.2 %) contents, the austenitic phase of 316L SS is stable at room temperature, and no transformation from austenite to martensite occurs, despite of the fast-cooling rate. These observations suggest that the temperature was above the recrystallization temperature during IFW for both materials, which is in agreement with the predicted temperature distributions (see Fig. 3) where the maximum temperature in the WZ was predicted to be ~1352 and 1339 °C for A516 and SS316L, respectively. The TMAZ of A516 steel (Fig. 5c) exhibited all three phases i.e., bainite, ferrite and pearlite while it's HAZ (Fig. 5d) consisted of ferrite and pearlite only (i.e., lower temperatures were reached during IFW). For the SS316L, microstructures of the TMAZ and HAZ (Fig. 5f and g, respectively) were found to be similar to that of the BM. The EBSD phase map (Fig. 5h) and its corresponding inverse pole-figure (IPF) map with respect to the AD direction (Fig. 5i) show an increase in grain size from WZ towards HAZ, which is also supported by the SEM observations (see Fig. 5b to g). No distinct boundary was observed at the weld interface due to a significant amount of materials intermixing as a result of severe plastic deformation. The geometrically necessary dislocation (GND) density map which is an indirect measurement of crystal distortion due to plastic deformation and the stored energy (Peng et al., 2022; Pantleon, 2008) is shown in Fig. 5j across different weld regions. The measurement of GND via EBSD maps is reported elsewhere (Konijnenberg et al., 2015). The GND density appears to be higher near the interface (WZ) indicating a higher level of strain energy. It is understood that the presence of martensite has a substantial effect on hindering dislocation mobility (Maki, 2012). The higher amount of martensite formation in the WZ of A516 steel leads to dislocation accumulation at the vicinity of the interfaces, therefore, high level of remaining dislocation which has not been annihilated as a result of the heat generated by the IFW. On the other hand, less amount of martensite was observed in the TMAZ, and no evidence of martensite was noticed in the HAZ and BM. This explanation serves as the potential reason for the decrease in the GND density in the TMAZ compared to the WZ. Comparatively, the GND density in the 316L side measured to be lower which is an indication of lower level of plastic strain. Although the deformation level in the 316L side could have been higher during IFW, owing to its austenitic crystal structure, it must have been annealed, due to the high temperature, on cooling.

Conclusions

In summary, the in-process evolution of temperature and stress during IFW of dissimilar steels were investigated by FE simulation. The maximum temperatures reached during the IFW for the A516 steel and SS316L were predicted as ~ 1352 and 1339 °C, respectively. The simulated results were in good agreement with the experimental findings in terms of flash profile, angular velocity and upset, thus implying the merit of the developed FE model to simulate the IFW process of dissimilar steels. No defects and cracks were observed in the actual weld apart from intermixing of the materials due to severe plastic deformation. The microstructure in the WZ of A516 steel consisted of martensite and granular bainite, while that of 316L showed small equiaxed austenitic grains. These observations were in agreement with the predicted temperature distribution by the FE model where the temperature in the WZ was above the recrystallization temperature. The drawn conclusions suggest the potential of this model to capture transient behaviors (both thermal and stress) during IFW of dissimilar steels.

Funding

This project received funding from the UK's High-Value Manufacturing CATAPULT.

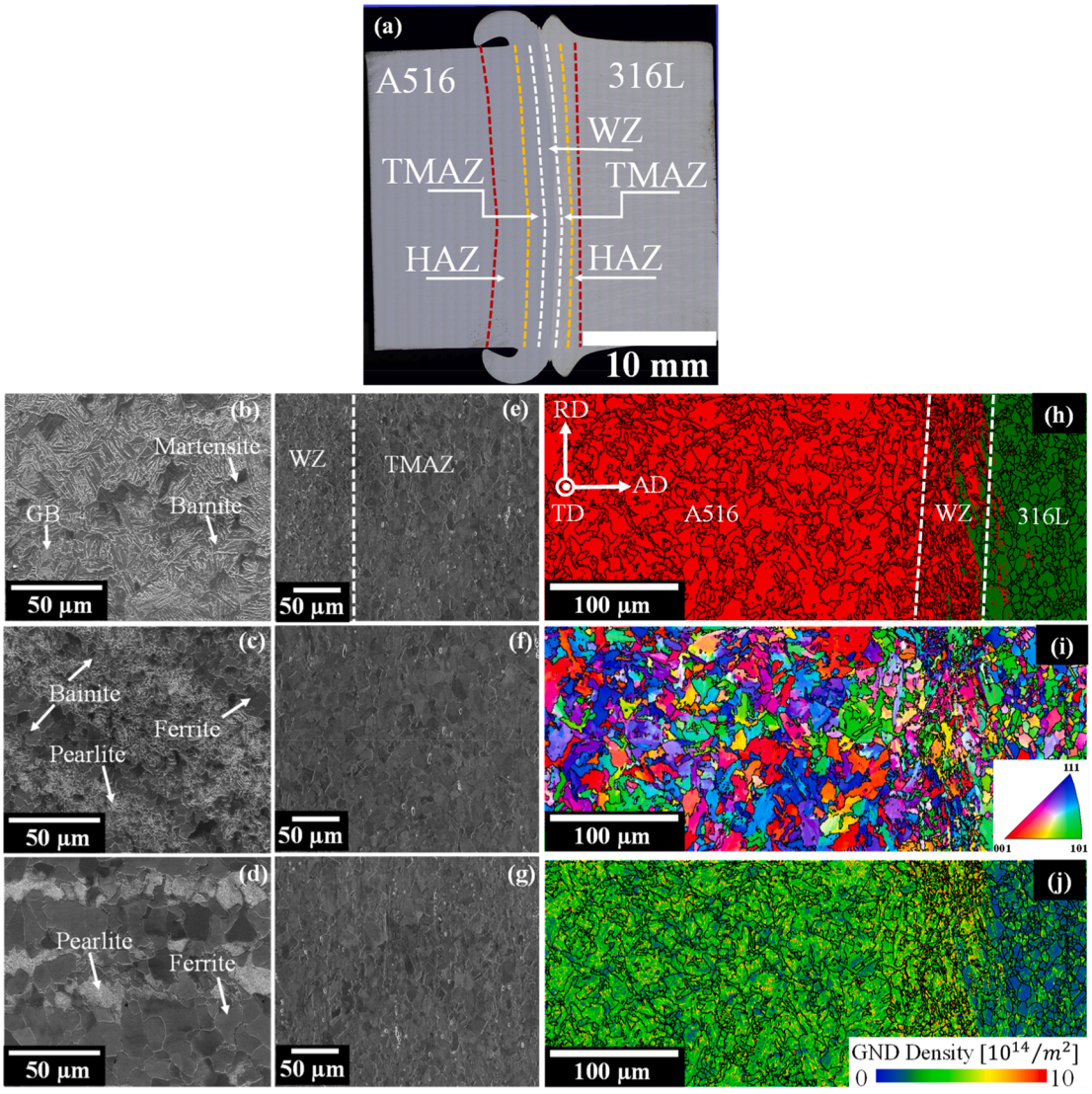

Fig. 5. (a) Macro image of the weld joint, (b), (c) and (d) SEM micrographs of A516 steel taken from the WZ, TMAZ and HAZ respectively, (e) – (g) SEM micrographs of SS316L for the WZ, TMAZ and HAZ respectively, (h) EBSD phase map, (i) IPF with respect to the AD direction, and (j) GND density map across different regions of the weld.

Declaration of Competing Interest

The authors declare that they have no known competing financial interests or personal relationships that could have appeared to influence the work reported in this paper.

Data availability

Data will be made available on request.

Acknowledgments

The authors would like to acknowledge the lab support provided by the Advanced Forming Research Centre (AFRC) at the University of Strathclyde, which receives partial financial support from the UK's High-Value Manufacturing CATAPULT. Kornelia Kondziolka is acknowledged for preparing the metallurgical specimens.

References

Balasubramanian, V., Li, Y., Stotler, T., Crompton, J., Soboyejo, A., Katsube, N., Soboyejo, W., 1999. A new friction law for the modelling of continuous drive friction welding: applications to 1045 steel welds. Mater. Manuf. Process. 14 (6), 845–860.

Banerjee, A., Ntovas, M., Da Silva, L., Rahimi, S., Wynne, B., 2021. Inter-relationship between microstructure evolution and mechanical properties in inertia friction welded 8630 low-alloy steel. Arch. Civ. Mech. Eng. 21 (4), 149.

Banerjee, A., Wylie, A., Da Silva, L., 2022. Near-net shape manufacture of ultra-high strength maraging steel using flow forming and inertia friction welding: experimental and microstructural characterization. J. Manuf. Sci. Eng. 145 (2).

Bennett, C.J., Attallah, M.M., Preuss, M., Shipway, P.H., Hyde, T.H., Bray, S., 2013. Finite element modeling of the inertia friction welding of dissimilar high-strength steels. Metall. Mater. Trans. A 44 (11), 5054–5064.

Cerjak, H., Bhadeshia, H., Kozeschnik, E., 2005. Mathematical Modelling of Weld Phenomena 7. Verlag der Technischen Universität Graz.

El-Hadek, M.A., 2014. Numerical simulation of the inertia friction welding process of dissimilar materials. Metall. Mater. Trans. B 45 (6), 2346–2356.

Geng, P., Qin, G., Zhou, J., 2019. Numerical and experimental investigation on friction welding of austenite stainless steel and middle carbon steel. J. Manuf. Process. 47, 83–97.

Ghosh, N., Pal, P.K., Nandi, G., 2018. Investigation on dissimilar welding of AISI 409 ferritic stainless steel to AISI 316L austenitic stainless steel by using grey based Taguchi method. Adv. Mater. Process. Technol. 4 (3), 385–401.

Konijnenberg, P.J., Zaefferer, S., Raabe, D., 2015. Assessment of geometrically necessary dislocation levels derived by 3D EBSD. Acta Mater. 99, 402–414.

Lee, K., Samant, A., Wu, W.T., Srivatsa, S., 2001. Finite element modeling of inertia welding processes. Proceedings of the NUMIFORM Conference. Japan, pp. 1095–1100.
Maalekian, M., Kozeschnik, E., Brantner, H.P., Cerjak, H., 2008. Comparative analysis of heat generation in friction welding of steel bars. Acta Mater. 56 (12), 2843–2855.
Maki, T., Pereloma, E., Edmonds, D.V., 2012. 2 - Morphology and substructure of martensite in steels. Phase Transformations in Steels. Woodhead Publishing, pp. 34–58.
Moal, A., Massoni, E., 1995. Finite element simulation of the inertia welding of two similar parts. Eng. Comput. 12 (6), 497–512.
Pantleon, W., 2008. Resolving the geometrically necessary dislocation content by conventional electron backscattering diffraction. Scr. Mater. 58 (11), 994–997.
Peng, H., Baker, I., Yi, Y., Hu, L., Fang, W., Li, L., Luo, B., Luo, Z., 2022. Dissimilar electron beam welding of the medium-entropy alloy $(NiCoCr)_{94}Al_3Ti_3$ to 304 stainless steel. Scr. Mater. 214, 114659.
Rathod, D.W., Pandey, S., Singh, P.K., Prasad, R., 2015. Experimental analysis of dissimilar metal weld joint: ferritic to austenitic stainless steel. Mater. Sci. Eng. A 639, 259–268.
Sunilkumar, D., Muthukumaran, S., Vasudevan, M., Reddy, M.G., 2020. Effect of friction stir and activated-GTA welding processes on the 9Cr–1Mo steel to 316LN stainless steel dissimilar weld joints. Sci. Technol. Weld. Join. 25 (4), 311–319.
Tung, D.J., Mahaffey, D.W., Senkov, O.N., Semiatin, S.L., Zhang, W., 2019. Transient behaviour of torque and process efficiency during inertia friction welding. Sci. Technol. Weld. Join. 24 (2), 136–147.
Vill, V.I., 1962. Friction Welding of Metals. Reinhold Publishing Company. American Welding Society; trade distributor.
Wang, H.T., Wang, G.Z., Xuan, F.Z., Tu, S.T., 2013. Fracture mechanism of a dissimilar metal welded joint in nuclear power plant. Eng. Fail. Anal. 28, 134–148.
Yang, X., Li, W., Li, J., Xiao, B., Ma, T., Huang, Z., Guo, J., 2015. Finite element modeling of the linear friction welding of GH4169 superalloy. Mater. Des. 87, 215–230.
Zhang, Q.Z., Zhang, L.W., Liu, W.W., Zhang, X.G., Zhu, W.H., Qu, S., 2006. 3D rigid viscoplastic FE modelling of continuous drive friction welding process. Sci. Technol. Weld. Join. 11 (6), 737–743.